Electrically Conductive Thermally Insulating Bi-Si Nanocomposites by Interface Design for Thermal Management

Yen-Ju Wu, Michiko Sasaki, Masahiro Goto, Lie Fang, Yibin Xu*

Center for Materials research by Information Integration (CMI2)

Research and Services Division of Materials Data and Integrated System (MaDIS)

National Institute for Materials Science (NIMS)

1-2-1 Sengen, Tsukuba, Ibaraki 305-0047, JAPAN

Email*: XU.Yibin@nims.go.jp

Key word: Thermal insulating thin film, Interface thermal resistance, Interface design, Nanostructuring, Nanocomposite, Machine learning

Abstract

We demonstrate, both by experiments and by data informatics, an alternative strategy to achieve ultralow thermal conductivity in a dense solid. The interfacial thermal resistance (ITR) prediction of machine learning model is implemented in a nanoscale field. The size dependence on ITR is considered and applied to the interface design of nanostructuring. The Bi/Si system was selected from 2025 kinds of interfaces through the interface thermal resistance prediction model by machine learning. The BiSi nanocomposite, which was composed of crystallized Bi and amorphous Si, was designed with various parameters by a laboratory-built combinatorial sputtering system. Electrically conductive, thermally insulating BiSi nanocomposites reported for the first time and have a thermal conductivity as low as 0.16 $Wm^{-1}K^{-1}$. The ultralow thermal conductivity is attributed to the high ratio between the interfacial surface area and the volume because of the small Bi particle size and high Si/Bi atomic ratio. By introducing the informatics method, the potential candidates can be discovered and realized for thermoelectric applications.

Introduction

Nanostructuring has become a potential option in the design of materials due to the unique electrical and thermal properties.[1-11] The nanostructures design can provide ultralow thermal conductivity as phonon propagation in such structures is hindered. The heat can be carried by phonons to dissipate through various vibrational modes; however, the phonons scatter into random directions or associated interferences when they encounter grain boundaries or interfaces inside nanostructured materials. As a result, the heat conduction paths are impeded, resulting in high thermal resistance, which can be exploited for thermal insulating films, high efficiency turbine coatings, and thermoelectric devices. Nanolaminates or superlattices that consist of alternating thin films without porous defects are attractive and promising, especially because of their good mechanical characteristics. Periodic nanolaminates or superlattice nanowires such as Si/Ge,[12-16] Ge/SiGe,[17] Si/SiGe,[18-21] GaAs/AlAs,[22-25], Bi_2Te_3/Sb_2Te_3,[26-28] W/Al_2O_3,[29] Ta/TaO_x,[30] $Ge_2Sb_2Te_5/ZnS:SiO_2$,[31] Mo/Si,[32] and Au/Si[33] have been proposed; in some cases, they have been demonstrated to have a thermal conductivity perpendicular to the multilayers even lower than that of homogeneous amorphous structure and the theoretical predicted values. As the distances between interfaces decrease, the reduction effect on thermal conductivity increases.[34] Therefore, the issue of how to realize this effect more efficiently has arisen. Interface design nanostructuring and synthesis and the selection of the materials system have become main issues to be addressed toward this goal.

Researchers have proposed various methods to select the candidates for interface design, Lee and Cahill have reported a correlation between the sound velocity ratio and thermal conductivity, specifically, they reported that Si/Ge superlattices, which have a higher ratio of 1.7, exhibit a lower thermal conductivity than GaAs/AlAs superlattices, which have a ratio of 1.2.[12] Another approach to identifying candidates—predicting the interfacial thermal resistance (ITR)—has led to the identification of models such as the acoustic mismatch model, the diffuse mismatch model, and molecular dynamics. A comparison of different prediction methods and details is presented elsewhere.[35] Although these models can aid in evaluating various materials systems, the ITR prediction is a high-dimensional problem that includes chemical, physical, and process factors that are not easily considered simultaneously.

Materials design

In this work, we introduce a direct and efficient way to select the materials from among hundreds of thousands of systems by the ITR prediction model through machine learning. Machine learning was used to predict ITR on the basis of experimental data; in this study, the machine learning was conducted with 746 data entries composed of 125 interface types and 35 materials, including metals, semiconductors and insulators, collected from 56 published papers. The references to the complete datasets are detailed in a previous study.[35] A detailed discussion of the machine learning model for ITR prediction, including the selection of the dataset, descriptors, and the algorithms, will be published soon. The ITR prediction model considers the physical, chemical, and process factors categorized into three main sets of descriptors: property descriptors, compound descriptors, and process descriptors; more importantly, the size dependence is also considered.[36] That is, the ITR prediction of a nanoscale field can be manipulated for nanostructuring design. The property descriptors (density, melting point, unit cell volume, and heat capacity), the compound descriptor for the interface conditions (atomic coordinates, electronegativity, ionization potential, mass, and binding energy), and process descriptors (thickness, interlayer) are input as descriptors for machine learning. While the initial algorithm settings are implemented in Matlab, the details are available elsewhere.[35] The entire dataset was randomly separated into five folds that were orthogonal to each other. The five-fold cross validation was conducted to generate optimized hyperparameters for the model and to estimate the fluctuations between each data fold. The correlation coefficient (R) and the root-mean-squared error (RMSE) were used to evaluate the models among various algorithms such as support vector machines, Gaussian regression processes, and regression tree ensembles of LSBoost. Here, the algorithms of regression tree ensembles of LSBoost was used, resulting in an R and RMSE of 0.93 and 11.9×10^{-9} m^2KW^{-1}, respectively. The correlation between the target and the prediction is shown in Figure 1(a). The mismatch between the target and the prediction is small and is suitable for further prediction. We next input 2025 kinds of interfaces (A/B) composed of 45 materials including metals, semiconductors, and insulators, with single element and binary compositions into the prediction model. The assumption used to select the materials system from the prediction rank was (1) high ITR and (2) no stable compound formation between the materials (A/B). By means of the clean interface without new compound or intermediate formation, the ITR effect was analyzed.

For the prediction of compound formation, we trained a prediction model using the categorized data of 15,419 from Villars et al.[37] The training data included 2016 binary (1382, 634), 7021 ternary (4274, 2747) and 6382 quaternary (4264, 2118) systems, with neglect of the contradictory information; values in the parentheses are the data number that form and that do not form a compound, respectively. In addition, the formation of a stable compound or intermediate was also checked using the data platforms of AtomWork Adv. and Material Project.[38-39]

On the basis of the aforementioned procedures, the Bi/Si system that exhibits a high ITR, does not form stable intermediates, and that can be practically manufactured was selected. Figure 1(b) shows the ITR prediction of Bi/Si from the machine learning model as a function of the thickness and temperature. At room temperature, the predictive ITR of Bi/Si without an interlayer and with a nanoscale thickness of 0.5 to 3 nm is 86.29×10^{-9} m^2KW^{-1}. The ITR value predicted from our machine learning model is very similar to the experimental result of 88.5×10^{-9} m^2KW^{-1} for a Bi/Si(100) interface, as reported by Cahill et al.[40] That is, the mismatch between the real experiments and this ITR predictive model is very small. An electrically conductive, thermally insulating BiSi hybrid nanocomposite is proposed for the first time. It shows promise as a hybrid system for thermoelectric materials or applications requiring electrical conductivity. To design the nanostructure with low thermal conductivity, more interfaces—specifically, a high ratio of interfacial surface area to volume (*S/V*)—can hinder heat transport and lead to lower thermal conductivity. Therefore, the Bi and Si materials were deposited alternatingly in order to restrict their sizes and thicknesses.

Experimental procedure

The samples of BiSi nanocomposites were prepared in laboratory-built combinatorial sputtering system, which can control fourteen parameters in the same chambers simultaneously.[41] The Bi and Si films with a few-nanometer thickness were deposited onto Si(100) substrates alternatingly and continuously, corresponding to various parameters such as Si-RF power, Si-target, and working pressure, as shown in Table 1. Samples 1-5 were prepared using an undoped-Si target, whereas samples 6-9 were prepared using a Si target doped with B at a concentration of 1.4×10^{19} cm^{-3}. The RF power was set at 100 W for Bi, whereas the RF power for Si was varied between 50 W and 100 W. The base pressure of the sputtering system is 3.75×10^{-7} Torr. The working pressure varied from 0.005 and 0.007 Torr, Ar was used as the sputtering gas, and the substrate temperature was maintained at room temperature (25°C). The RF power and working pressure affect the velocity and mean free path of the ions causing various ions to interact. Parameters h_{Bi} and h_{Si} are the thickness of Bi and Si corresponding to the quartz crystal resonator; the thicknesses of Si and Bi were increased from 0.5 to 3 nm. The nanoscale alternating deposition produced numerous Bi nanoparticles embedded in the Si matrix. In general, the Bi nanoparticles spread uniformly in the Si matrix; however, in some samples, local layered structures remained. The total film thickness and average Bi particle sizes were measured by scanning transmission electron microscopy (STEM). The atomic percentages (At%) were analyzed through energy-dispersive X-ray spectroscopy (EDX) with focused-ion beam (FIB) samples of 100-nm thickness. The FIB was carried out using a Hitachi FB-2100 (30 kV); the STEM was carried out using a Hitachi HD-2700 Cs-corrected STEM (200 kV), and a JEOL JEM 2100F (200 kV); the EDX was carried out using an AMETEK EDAX Octane T Ultra W (200 kV). After the Bi/Si deposition, a 120 nm-thick Au layer was deposited, without evacuation, at the top as a heat absorber for thermal resistance (*R*) measurement by frequency-domain thermoreflectance (FDTR).[42] The thermal resistance was along the perpendicular direction (cross-plane) to the Si substrate. By dividing the film thickness by *R*, we subsequently determined the thermal conductivity (κ_c) along cross-plane. The electrical conductivity (σ_i) and thermal conductivity (κ_i) along the direction parallel to the Si substrate (in-plane) of sample 6 were performed with the Linseis thin film analysis (TFA) system. And the electrical conductivity (σ_i) of other samples were measured through the four-point probe method. The details of experimental parameters and measured results are shown in Table 1.

Results and discussion

Figure 2(a) illustrates the structure of the system composed of an Au layer, the Bi/Si composite thin film, and a Si substrate. The samples with Au layer were only used for the FDTR measurement, whereas the samples without Au layer were used for other measurements, such as XRD. In the Bi/Si composite thin film, there are several Bi particles marked by the grey dashed line embedded in the Si-matrix. The small-angled XRD patterns of all of the samples at an incident angle of 0.5 ° are shown in Figure 2(b). The single dominant peak is Bi(012), space group is R-3mh (space group no. 166), defined from the NIMS database of AtomWorkAdv.[39] No Si peak is observed, indicating that the nanocomposite is composed of crystallized Bi and amorphous Si (a-Si), with no additional phase. The intensity of the dominant peak of sample 8, which was prepared at a lower working pressure, is relatively low compared with those of the other samples. By contrast, the pattern of sample 9, which was prepared at a lower RF power for Si, shows the highest peak intensity. The working pressure and RF power change the Bi and Si interaction by changing the velocity and mean free path of the source ions; the working pressure and RF power therefore change the crystallinity of Bi.

The thermal conductivity (κ_i) and electrical conductivity (σ_i) of sample 6 along the direction parallel to the Si substrate (in-plane) are plotted against the temperature in Figure 3. As the temperature increases from 123.3 K to 348.3 K, the electrical conductivity increases linearly from 1.98 to 4.66×10^2 S/cm, whereas the thermal conductivity increases from 1.04 to 1.7 $\mathrm{Wm^{-1}K^{-1}}$. The conductive property of the BiSi nanocomposites can benefit to various electronic devices. The electrical conductivity (σ_i) and thermal conductivity (κ_i) at room temperature of sample 6 is 3.94×10^2 S/cm and 1.65 $\mathrm{Wm^{-1}K^{-1}}$ in Figure 3, respectively. Although the Wiedemann–Franz law is reported to breakdown in nanoscale,[43-44] it is not further considered here. From the estimation based on the Wiedemann–Franz law, the thermal conductivity contributed by the electrons in the in-plane direction is 0.29 $\mathrm{Wm^{-1}K^{-1}}$. The in-plane thermal conductivities (κ_i) of sample 6 are around three times larger compared with the cross-plane thermal conductivity (κ_c) of 0.44 $\mathrm{Wm^{-1}K^{-1}}$.

The electrical conductivity (σ_i) at room temperature of sample 3 is 0.74×10^2 S/cm in Table 1. Based on the Wiedemann–Franz law, the thermal conductivity (κ_i) for samples 3 in the in-plane direction contributed by the electrons is 0.05 $\mathrm{Wm^{-1}K^{-1}}$, which is much smaller than that of 0.29

$Wm^{-1}K^{-1}$ for sample 6. The difference of sample preparation between sample 3 and 6 is that the Si target was changed from undoped-Si (samples 1-5) to a B-doped Si target (samples 6-9). These results imply that the B-doped Si target increases the thermal conductivity of the BiSi nanocomposites, which is consistent with the experimental thermal conductivity results shown in Table 1.

The B-doped Si target increases the electrical conductivity of BiSi samples by one order, however, the sample 9 deposited with B-doped Si has two-order differences compared with sample 6-8. The horizontal Bi particles dominantly contribute to the in-plane electrical conductivity, therefore, the sample 6 with large Bi particles has the highest electrical conductivity. The dark-field STEM images of sample 3, 6, and 9 can be found in Figure S2 of "supporting information." The large Bi aggregations in sample 3, as shown in Figure S2(a), may also contribute to the electrical conductivity. Although the sample 9 has similar Bi particle size along vertical direction with sample 3 and 5 in Table 1, the different shapes of Bi particles lead to different Bi particle sizes between cross-plane and in-plane directions. The Bi particles of sample 9, compared with sample 3 and 6 as shown in Figure S2, have more isotropic shapes and the shortest length in the in-plane direction. The in-plane electrical conductivity of sample 9 of 0.010×10^2 S/cm (Table 1) is only a bit higher than that of the B-doped Si thin film of 0.008×10^2 S/cm. It implies that the discontinuous small Bi particles in sample 9 contributes less to the in-plane electrical conductivity. As a result, the sample 9 has the lowest in-plane electrical conductivity among all the samples.

To further analyze the factors contributing to low thermal conductivity of the BiSi nanocomposites, we characterized their structures by bright-field STEM; the results are shown in Figure 4, where subfigures (a)-(g) correspond to samples 2, 3, 5, 7, 9, 6, and 8, respectively. In Figure 4. (a)-(e), numerous small Bi particles with diameters from 3 to 10 nm are uniformly spread in the thin films. In particular, for the samples 2, 3, and 5, which exhibit thermal conductivities less than 0.2 $Wm^{-1}K^{-1}$ in Figure 4(a)-(c), respectively, the a-Si (light-grey areas) is separated by many small Bi particles approximately 5 nm in diameter (black areas). In order to define the Bi particles clearly, several Bi particles are marked by the red squares for examples in each sample in Figure 4. By contrast, Figure 4(f) and (g), which correspond to samples 6 and 8, show several large Bi aggregations or particles distributed in the film. The particle sizes of Bi, as measured from STEM images, are plotted against the cross-plane thermal conductivity in Figure 5, where the numbers next to the data points are the sample ID numbers. The cross-plane thermal conductivity decreases with decreasing particle size, and the lowest thermal conductivity of 0.16 $Wm^{-1}K^{-1}$ is observed for sample 5. In the case where the particle size increases to greater than 10 nm (sample 6), the thermal conductivity substantially increases to 0.44 $Wm^{-1}K^{-1}$. High-resolution (HR) STEM dark-field images of samples 3, 7, and 6 are shown in Figure 6(a), (b), and (c), respectively, whereas the corresponding bright-field images are shown in larger scale in Figure 6(d), (e), and (f), respectively. The Bi particles are defined by the grey dashed lines in Figure 6(d), (e), and (f), and the average lengths along the vertical direction of three different STEM regions were measured as the Bi particle sizes for each sample as shown in Figure 5 and Table 1. The statistical histograms for Bi particle distribution of each sample are shown in "supporting information". The Bi exhibits a brighter color in the dark-field images and a darker color in the bright-field images. Figure 6(g) and (h) shows the diffraction pattern of a Bi particle and its corresponding fast Fourier transform (FFT) pattern in reciprocal space. The selected region of the Bi particle, marked by a red square in Figure 6(f), has a clear lattice structure along [001] direction determined through the FFT. The Bi particle was analyzed as bismuth trigonal phase, Bi(R-3mh), which corresponds to the XRD in Figure 2. The change in the Bi particle size from 4.33 nm in sample 3 to 6.39 nm in sample 7 and to 10.04 nm in sample 6 is evident in Figure 6. The hetero-interfaces can hinder the heat transfer and increase the thermal resistance.[27, 32, 34] Smaller Bi particles spreading in a-Si create additional interfaces: that is, the *S/V* ratio becomes high. The samples with smaller Bi particles thereby achieve a lower thermal conductivity consistent with the results in Figure 5.

As shown in Figure 5, sample 8 has a Bi particle size that is smaller than 7 nm but a high thermal conductivity of 0.42 $Wm^{-1}K^{-1}$. Figure 7 (a) and (d) show the bright-field HR-STEM images of sample 8, which is clearly composed of large Bi particles embedded in an a-Si matrix as well as in local layered-like structures. As shown in Figure 6 (b) and (e), compared with the thermal conductivity of sample 7, which has a similar particle size, the thermal conductivity of sample 8 is 1.68 times greater. The *S/V* ratio of spherical Bi particles is larger than that of the layered structure; thus, the spherical Bi particles can contribute more to the thermal resistance than the layered structure because of the random direction of heat transport. Moreover, the sample 6, which has several horizontal Bi particles embedded in an a-Si matrix as shown in Figure 4(f) and Figure 6(c), has higher in-plane thermal conductivity (Figure 3) than cross-plane thermal conductivity (Figure 5) by 3.8 times at room temperature. It is implied that the anisotropy of the structure between the in-plane and cross-plane directions may influence the thermal conductivity.[45-46] Since the sample 7 and 8 have similar shapes of Bi particles with sample 6 as shown in Figure 4(d), (f) and(g), they should also have the anisotropic structure dependence on thermal conductivity. On the other hand, the anisotropic grains, anisotropic particles, rods, or laminar structures, may also cause the anisotropic electrical conductivity as addressed in the research.[47-49] As a result, we believe the BiSi nanocomposites would have higher electrical conductivity along the in-plane directions.

Figure 7(b) and (e) show the bright-field and dark-field STEM images, respectively, of different regions of sample 3. Several large aggregations are observed in the film, near the Si substrates. The aggregations are Bi, as revealed through the EDX analysis results in Figure 7(c) and (d), corresponding to the selected region of Figure 7 (e). The red spots and blue spots represent

Bi and Si, respectively. On the contrary, no or few aggregations appear in samples 6-9, which were deposited using a B-doped Si target. The melting point of Bi, 271.5 °C, is not high; thus, when the temperature increases during sputtering deposition, Bi tends to evaporate or to diffuse to lower temperature regions. The B-doped Si increases the electrical conductivity and thermal conductivity of the sample and therefore reduces the temperature gradient perpendicular to the Si substrate. Sample 1-5 have rather steep temperature gradients compared with sample 6-9 in the direction perpendicular to the substrate; these large gradients induce Bi to diffuse from the surface to the lower-temperature Si substrate and to form large Bi aggregations near the substrate. Consequently, in samples 6-9, Bi is assumed to form Bi particles that spread throughout in the film instead of forming large Bi aggregations near the Si substrate. In addition, the Si/Bi atomic ratios listed in Table 1, shows that sample 3, which was prepared using an undoped-Si target, has an Si/Bi atomic ratio of 3.65. This is higher than the corresponding ratios of samples 6-8, which were deposited using a B-doped Si target. The Bi At% in most regions that contributed to the increase of thermal resistance decreases, resulting from the existence of Bi aggregations. As a result, the difference in the aforementioned Si/Bi atomic ratio is attributed to the formation of Bi aggregations. Among sample 6-8, some local fluctuations from experimental parameters or Bi diffusion occur; these fluctuations cause the Si/Bi atomic ratio to range between 1.55 and 2.42.

Figure 8(a) shows the Si and Bi At% as functions of the thermal conductivity, where red circles represent Si At% and black squares represent Bi At%. Samples 3, 7, 8, and 6 are labeled near the red curve of Si At%. With an increasing Si/Bi atomic ratio, the thermal conductivity decreases. The main factor by which the Si/Bi atomic ratio affects the thermal conductivity is the difference in intrinsic thermal conductivity between Bi and Si. The intrinsic thermal conductivity of Bi and a-Si are 8 and 0.93 $Wm^{-1}K^{-1}$, respectively. Thus, BiSi nanocomposites with a higher Si At% tend to exhibit a lower thermal conductivity.

Figure 8(b) summarizes the thermal conductivities of several inorganic material systems with nanostructured-design, including Si/SiGe,[18] GaAs/AlAs,[25] Si/Ge superlattice nanowires (SLNWs),[13] W/Al_2O_3,[29] Ta/TaO_x,[30] Mo/Si,[32] $Ge_2Sb_2Te_5$/ZnS:SiO_2,[31] Au/Si,[33] and Bi_2Te_3/Sb_2Te_3.[26] The thermal conductivity ranges from 0.25 to 9.6 $Wm^{-1}K^{-1}$. The BiSi nanocomposites proposed in this work labeled as green triangles exhibit the lowest thermal conductivity of 0.16 $Wm^{-1}K^{-1}$. The ideal parameter range for BiSi nanocomposite is defined and an extremely low thermal conductivity in condense materials field is achieved. The small particle size of Bi spreading in the a-Si matrix and the high Si/Bi atomic ratio both hinder heat transport. The high *S/V* ratio through the interface design can successfully decrease the thermal conductivity. In addition, the designed thermally insulating BiSi nanocomposites are electrically conductive, unlike other low-thermal-conductivity materials, and have a strong potential in applications that require materials with good electrical conductivity, such as thermoelectric devices.

Conclusion

Electrically conductive thermally insulating BiSi nanocomposites were demonstrated through interface design, data informatics, and a laboratory-built combinatorial sputtering system. The Bi/Si system was selected from the ITR predictive model by machine learning. The BiSi nanocomposites were composed of crystallized Bi and amorphous Si. The ultralow thermal conductivity was attributed to the high *S/V* ratio of Si/Bi, consistent with the small Bi particles uniformly spreading in an a-Si with a high Si/Bi atomic ratio. The electrically conductive thermally insulating BiSi nanocomposites are proposed for the first time. They feature an ultralow thermal conductivity of 0.16 $Wm^{-1}K^{-1}$ and an anisotropic thermal property. The combination of a machine learning prediction model and an interface design enable the discovery and realization of potential systems for specific thermal management, such as thermoelectric materials.

Acknowledgment

This work was supported by the "Materials research by Information Integration" Initiative (MI2I) project of the Support Program for Starting Up Innovation Hub from Japan Science and Technology Agency. We would also like to show our gratitude to Vincent Linseis and Florian Linseis, Linseis Thermal Analysis Germany, for the measurement support of electrical and thermal conductivities along in-plane direction. We thank Prof. Pierre Villars, Material Phases Data System (MPDS), for sharing their dataset of the compound formation. The STEM, FIB, EDX analysis were supported by the Namiki Foundry of National Institute for Materials Science (NIMS).

Additional Information

The authors declare that they have no significant competing financial, professional or personal interests that might have influenced the performance or presentation of the work described in this manuscript.

References

1. Liu, H.; Gao, J.; Huang, W.; Dai, K.; Zheng, G.; Liu, C.; Shen, C.; Yan, X.; Guo, J.; Guo, Z., Electrically conductive strain sensing polyurethane nanocomposites with synergistic carbon nanotubes and graphene bifillers. *Nanoscale* **2016,** *8* (26), 12977-12989.
2. Liu, H.; Huang, W.; Gao, J.; Dai, K.; Zheng, G.; Liu, C.; Shen, C.; Yan, X.; Guo, J.; Guo, Z., Piezoresistive behavior of porous carbon nanotube-thermoplastic polyurethane conductive nanocomposites with ultrahigh compressibility. *Applied Physics Letters* **2016,** *108* (1), 011904.
3. Liu, H.; Huang, W.; Yang, X.; Dai, K.; Zheng, G.; Liu, C.; Shen, C.; Yan, X.; Guo, J.; Guo, Z., Organic vapor sensing behaviors of conductive thermoplastic polyurethane-graphene nanocomposites. *Journal of Materials Chemistry C* **2016,** *4* (20), 4459-4469.
4. Hu, C.; Li, Z.; Wang, Y.; Gao, J.; Dai, K.; Zheng, G.; Liu, C.; Shen, C.; Song, H.; Guo, Z., Comparative assessment of the strain-sensing behaviors of polylactic acid nanocomposites: reduced graphene oxide or carbon nanotubes. *Journal of Materials Chemistry C* **2017,** *5* (9), 2318-2328.
5. Huang, W.; Dai, K.; Zhai, Y.; Liu, H.; Zhan, P.; Gao, J.; Zheng, G.; Liu, C.; Shen, C., Flexible and Lightweight Pressure Sensor Based on Carbon Nanotube/Thermoplastic Polyurethane-Aligned Conductive Foam with Superior Compressibility and Stability. *ACS Applied Materials & Interfaces* **2017,** *9* (48), 42266-42277.
6. Liu, H.; Dong, M.; Huang, W.; Gao, J.; Dai, K.; Guo, J.; Zheng, G.; Liu, C.; Shen, C.; Guo, Z., Lightweight conductive graphene/thermoplastic polyurethane foams with ultrahigh compressibility for piezoresistive sensing. *Journal of Materials Chemistry C* **2017,** *5* (1), 73-83.
7. Wei, X.; Cao, X.; Wang, Y.; Zheng, G.; Dai, K.; Liu, C.; Shen, C., Conductive herringbone structure carbon nanotube/thermoplastic polyurethane porous foam tuned by epoxy for high performance flexible piezoresistive sensor. *Composites Science and Technology* **2017,** *149*, 166-177.
8. Zhang, M.; Liu, E.; Cao, T.; Wang, H.; Shi, C.; Li, J.; He, C.; He, F.; Ma, L.; Zhao, N., Sandwiched graphene inserted with graphene-encapsulated yolk-shell [gamma]-Fe2O3 nanoparticles for efficient lithium ion storage. *Journal of Materials Chemistry A* **2017,** *5* (15), 7035-7042.
9. Li, Y.; Zhou, B.; Zheng, G.; Liu, X.; Li, T.; Yan, C.; Cheng, C.; Dai, K.; Liu, C.; Shen, C.; Guo, Z., Continuously prepared highly conductive and stretchable SWNT/MWNT synergistically composited electrospun thermoplastic polyurethane yarns for wearable sensing. *Journal of Materials Chemistry C* **2018,** *6* (9), 2258-2269.
10. Wang, Y.; Hao, J.; Huang, Z.; Zheng, G.; Dai, K.; Liu, C.; Shen, C., Flexible electrically resistive-type strain sensors based on reduced graphene oxide-decorated electrospun polymer

fibrous mats for human motion monitoring. *Carbon* **2018,** *126*, 360-371.

11. Zheng, Y.; Li, Y.; Dai, K.; Wang, Y.; Zheng, G.; Liu, C.; Shen, C., A highly stretchable and stable strain sensor based on hybrid carbon nanofillers/polydimethylsiloxane conductive composites for large human motions monitoring. *Composites Science and Technology* **2018,** *156*, 276-286.
12. Lee, S. M.; Cahill, D. G.; Venkatasubramanian, R., Thermal conductivity of Si–Ge superlattices. *Applied Physics Letters* **1997,** *70* (22), 2957-2959.
13. Hu, M.; Poulikakos, D., Si/Ge Superlattice Nanowires with Ultralow Thermal Conductivity. *Nano Letters* **2012,** *12* (11), 5487-5494.
14. Bulusu, A.; Walker, D. G., Quantum Modeling of Thermoelectric Properties of Si/Ge/Si Superlattices. *IEEE Transactions on Electron Devices* **2008,** *55* (1), 423-429.
15. Borca-Tasciuc, T.; Liu, W.; Liu, J.; Zeng, T.; Song, D. W.; Moore, C. D.; Chen, G.; Wang, K. L.; Goorsky, M. S.; Radetic, T.; Gronsky, R.; Koga, T.; Dresselhaus, M. S., Thermal conductivity of symmetrically strained Si/Ge superlattices. *Superlattices and Microstructures* **2000,** *28* (3), 199-206.
16. Lin, K.-H.; Strachan, A., Thermal transport in SiGe superlattice thin films and nanowires: Effects of specimen and periodic lengths. *Physical Review B* **2013,** *87* (11), 115302.
17. Chrastina, D.; Cecchi, S.; Hague, J. P.; Frigerio, J.; Samarelli, A.; Ferre–Llin, L.; Paul, D. J.; Müller, E.; Etzelstorfer, T.; Stangl, J.; Isella, G., Ge/SiGe superlattices for nanostructured thermoelectric modules. *Thin Solid Films* **2013,** *543*, 153-156.
18. Huxtable, S. T.; Abramson, A. R.; Tien, C.-L.; Majumdar, A.; LaBounty, C.; Fan, X.; Zeng, G.; Bowers, J. E.; Shakouri, A.; Croke, E. T., Thermal conductivity of Si/SiGe and SiGe/SiGe superlattices. *Applied Physics Letters* **2002,** *80* (10), 1737-1739.
19. Wu, Y.; Fan, R.; Yang, P., Block-by-Block Growth of Single-Crystalline Si/SiGe Superlattice Nanowires. *Nano Letters* **2002,** *2* (2), 83-86.
20. Kasper, E., Growth and properties of Si/SiGe superlattices. *Surface Science* **1986,** *174* (1), 630-639.
21. Li, D.; Wu, Y.; Fan, R.; Yang, P.; Majumdar, A., Thermal conductivity of Si/SiGe superlattice nanowires. *Applied Physics Letters* **2003,** *83* (15), 3186-3188.
22. Yu, X. Y.; Chen, G.; Verma, A.; Smith, J. S., Temperature dependence of thermophysical properties of GaAs/AlAs periodic structure. *Applied Physics Letters* **1995,** *67* (24), 3554-3556.
23. Daly, B. C.; Maris, H. J., Calculation of the thermal conductivity of superlattices by molecular dynamics simulation. *Physica B: Condensed Matter* **2002,** *316-317*, 247-249.
24. Capinski, W. S.; Maris, H. J.; Ruf, T.; Cardona, M.; Ploog, K.; Katzer, D. S., Thermal-conductivity measurements of GaAs/AlAs superlattices using a picosecond optical pump-and-probe technique. *Physical Review B* **1999,** *59* (12), 8105-8113.

25. Luckyanova, M. N.; Johnson, J. A.; Maznev, A. A.; Garg, J.; Jandl, A.; Bulsara, M. T.; Fitzgerald, E. A.; Nelson, K. A.; Chen, G., Anisotropy of the Thermal Conductivity in GaAs/AlAs Superlattices. *Nano Letters* **2013,** *13* (9), 3973-3977.

26. Touzelbaev, M. N.; Zhou, P.; Venkatasubramanian, R.; Goodson, K. E., Thermal characterization of Bi2Te3/Sb2Te3 superlattices. *Journal of Applied Physics* **2001,** *90* (2), 763-767.

27. König, J. D.; Winkler, M.; Buller, S.; Bensch, W.; Schürmann, U.; Kienle, L.; Böttner, H., Bi2Te3-Sb2Te3 Superlattices Grown by Nanoalloying. *Journal of Electronic Materials* **2011,** *40* (5), 1266-1270.

28. Wang, Y.; Liebig, C.; Xu, X.; Venkatasubramanian, R., Acoustic phonon scattering in Bi2Te3/Sb2Te3 superlattices. *Applied Physics Letters* **2010,** *97* (8), 083103.

29. Costescu, R. M.; Cahill, D. G.; Fabreguette, F. H.; Sechrist, Z. A.; George, S. M., Ultra-low thermal conductivity in W/Al2O3 nanolaminates. *Science* **2004,** *303* (5660), 989-90.

30. Ju, Y. S.; Hung, M. T.; Carey, M. J.; Cyrille, M. C.; Childress, J. R., Nanoscale heat conduction across tunnel junctions. *Applied Physics Letters* **2005,** *86* (20), 203113.

31. Kim, E. K.; Kwun, S. I.; Lee, S. M.; Seo, H.; Yoon, J. G., Thermal boundary resistance at Ge2Sb2Te5/ZnS:SiO2 interface. *Applied Physics Letters* **2000,** *76* (26), 3864-3866.

32. Bozorg-Grayeli, E.; Li, Z.; Asheghi, M.; Delgado, G.; Pokrovsky, A.; Panzer, M.; Wack, D.; Goodson, K. E., Thermal conduction properties of Mo/Si multilayers for extreme ultraviolet optics. *Journal of Applied Physics* **2012,** *112* (8), 083504.

33. Dechaumphai, E.; Lu, D.; Kan, J. J.; Moon, J.; Fullerton, E. E.; Liu, Z.; Chen, R., Ultralow thermal conductivity of multilayers with highly dissimilar Debye temperatures. *Nano Lett* **2014,** *14* (5), 2448-55.

34. Chiritescu, C.; Cahill, D. G.; Nguyen, N.; Johnson, D.; Bodapati, A.; Keblinski, P.; Zschack, P., Ultralow thermal conductivity in disordered, layered WSe2 crystals. *Science* **2007,** *315* (5810), 351-3.

35. Zhan, T.; Fang, L.; Xu, Y., Prediction of thermal boundary resistance by the machine learning method. *Scientific Reports* **2017,** *7* (1), 7109.

36. Xu, Y.; Kato, R.; Goto, M., Effect of microstructure on Au/sapphire interfacial thermal resistance. *Journal of Applied Physics* **2010,** *108* (10), 104317.

37. Pierre VILLARS, J. D., Yoshihiro SHIKATA, Krishna RAJAN, Shuichi IWATA, A new approach to describe elemental-property parameters. *Chemistry of Metals and Alloys* **2008,** *1*, 1-23.

38. Jain, A.; Ong, S. P.; Hautier, G.; Chen, W.; Richards, W. D.; Dacek, S.; Cholia, S.; Gunter, D.; Skinner, D.; Ceder, G.; Persson, K. A., Commentary: The Materials Project: A materials genome approach to accelerating materials innovation. *APL Materials* **2013,** *1* (1), 011002.

39. Inorganic Material Database (AtomWork-adv). NIMS Materials Database (MatNavi): 2017.

40. Lyeo, H.-K.; Cahill, D. G., Thermal conductance of interfaces between highly dissimilar materials. *Physical Review B* **2006,** *73* (14), 144301.

41. Goto, M.; Sasaki, M.; Xu, Y.; Zhan, T.; Isoda, Y.; Shinohara, Y., Control of p-type and n-type thermoelectric properties of bismuth telluride thin films by combinatorial sputter coating technology. *Applied Surface Science* **2017,** *407*, 405-411.

42. Xu, Y. B.; Wang, H. T.; Tanaka, Y.; Shimono, M.; Yamazaki, M., Measurement of interfacial thermal resistance by periodic heating and a thermo-reflectance technique. *Mater Trans* **2007,** *48* (2), 148-150.

43. Zhang, Q. G.; Cao, B. Y.; Zhang, X.; Fujii, M.; Takahashi, K., Size effects on the thermal conductivity of polycrystalline platinum nanofilms. *Journal of Physics: Condensed Matter* **2006,** *18* (34), 7937.

44. Ou, M. N.; Yang, T. J.; Harutyunyan, S. R.; Chen, Y. Y.; Chen, C. D.; Lai, S. J., Electrical and thermal transport in single nickel nanowire. *Applied Physics Letters* **2008,** *92* (6), 063101.

45. Xu, Y. B.; Kinugawa, J.; Yagi, K., Constitutional dependence of thermal conductivity in dispersion composites. *Mater Trans* **2003,** *44* (9), 1709-1712.

46. Xu, Y. B.; Yagi, K., Calculation of the thermal conductivity of randomly dispersed composites using a finite element modelling method. *Mater Trans* **2004,** *45* (8), 2602-2605.

47. Carmona, F.; El Amarti, A., Anisotropic electrical conductivity in heterogeneous solids with cylindrical conducting inclusions. *Physical Review B* **1987,** *35* (7), 3284-3290.

48. Lee, M. S.; Kim, T. Y.; Kim, D., Anisotropic electrical conductivity of delafossite-type CuAlO2 laminar crystal. *Applied Physics Letters* **2001,** *79* (13), 2028-2030.

49. Peng, H.; Xie, C.; Schoen, D. T.; Cui, Y., Large anisotropy of electrical properties in layer-structured In2Se3 nanowires. *Nano Lett* **2008,** *8* (5), 1511-6.

Captions of Tables

Table 1 The experimental parameters and measured properties of BiSi nanocomposites labeled as samples 1-9. The h_{Bi} and h_{Si} are the thicknesses of Bi and Si corresponding to the quartz crystal resonator, respectively. The thermal resistance (*R*) was measured by frequency-domain thermoreflectance (FDTR) along the perpendicular direction (cross-plane). The Bi particle size and film thickness were measured by STEM. The average lengths along the vertical direction of three different STEM regions were measured as the Bi particle sizes for each sample. The thermal conductivity (κ_c) was evaluated by dividing the film thickness by *R*. The electrical conductivity (σ_i) along the direction parallel to the Si substrate (in-plane) were measured by four-point probe method.

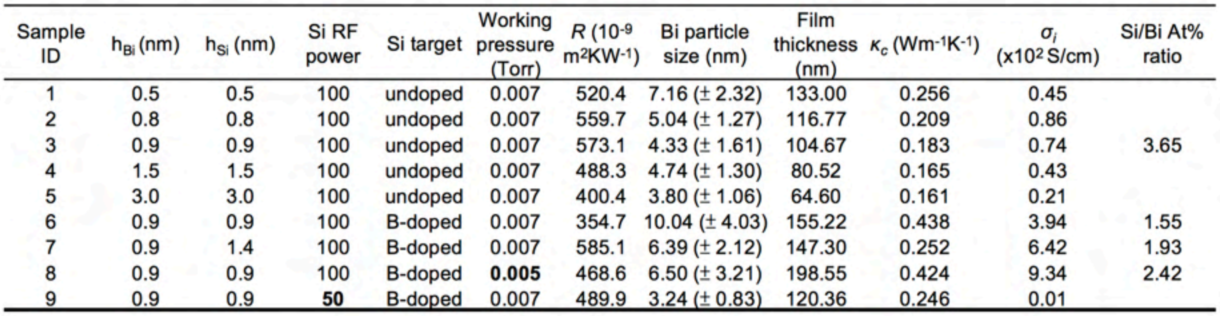

Sample ID	h_{Bi} (nm)	h_{Si} (nm)	Si RF power	Si target	Working pressure (Torr)	*R* (10^{-9} m^2KW^{-1})	Bi particle size (nm)	Film thickness (nm)	κ_c ($Wm^{-1}K^{-1}$)	σ_i ($x10^2$ S/cm)	Si/Bi At% ratio
1	0.5	0.5	100	undoped	0.007	520.4	7.16 (± 2.32)	133.00	0.256	0.45	
2	0.8	0.8	100	undoped	0.007	559.7	5.04 (± 1.27)	116.77	0.209	0.86	
3	0.9	0.9	100	undoped	0.007	573.1	4.33 (± 1.61)	104.67	0.183	0.74	3.65
4	1.5	1.5	100	undoped	0.007	488.3	4.74 (± 1.30)	80.52	0.165	0.43	
5	3.0	3.0	100	undoped	0.007	400.4	3.80 (± 1.06)	64.60	0.161	0.21	
6	0.9	0.9	100	B-doped	0.007	354.7	10.04 (± 4.03)	155.22	0.438	3.94	1.55
7	0.9	1.4	100	B-doped	0.007	585.1	6.39 (± 2.12)	147.30	0.252	6.42	1.93
8	0.9	0.9	100	B-doped	**0.005**	468.6	6.50 (± 3.21)	198.55	0.424	9.34	2.42
9	0.9	0.9	**50**	B-doped	0.007	489.9	3.24 (± 0.83)	120.36	0.246	0.01	

Table 1

Captions of Figures

Figure 1 (a) The plot of ITR target (real data from the references) against ITR prediction (predicted data by the model). (b) The ITR prediction of Bi/Si interface from the machine learning model as functions of the thickness and temperature. The ITR prediction with or without interlayer are both shown, and the latter have higher ITR values than the former.

Figure 2 (a) The illustration of the system structure of Bi/Si nanocomposites. (b)The XRD of BiSi nanocompoites. All samples from 1 to 9 have a single dominant peak of Bi(012), whereas no peak is observed for Si.

Figure 3 The thermal conductivity (κ_i) and electrical conductivity (σ_i) along the direction parallel to the Si substrate (in-plane) of sample 6 are plotted against the temperature.

Figure 4 The bright-field STEM images of BiSi nanocomposites. (a) to (g) are samples 2, 3, 5, 7, 9, 6, and 8, respectively. The scale bar of 100 nm is on the right bottom. The sample IDs are labeled in white in each image. There are several Bi particles marked by the red squares to show the particle shapes in each sample.

Figure 5 The cross-plane thermal conductivity against Bi particle size of BiSi nanocomposites. The thermal conductivity increases with larger Bi particle size.

Figure 6 The HR-STEM images of samples 3, 7, and 6 in (a)(d), (b)(e), and (c)(f), respectively. Images (a), (b), and (c) are dark-field images, and (d), (e), and (f) are bright-field images. (g) and (h) are the diffraction patterns of Bi particles of the red square region in (f) and the corresponding fast Fourier transform (FFT) pattern with the [001] viewing direction, respectively. The Bi has brighter colors in the dark-field images and has darker colors in the bright-field images. The sample numbers are labeled in white in (a), (b), and (c).

Figure 7 The bright-field HR-STEM images of sample 8 are shown in (a) and (d). The bright-field and dark-field STEM images of sample 3 are shown in (b) and (e). The sample ID numbers are labeled in white in (a) and (b). The corresponding EDX images of (e) for Bi and Si are shown in (c) and (f), respectively.

Figure 8 (a) The Si, Bi At% plotted against thermal conductivity of BiSi nanocomposites. The red circles are Si At% and the black squares are Bi At%. (b) A comparison of the thermal conductivities with various material systems with nanostructuring design. The data with various parameters for each material system are all collected in this plot. The BiSi nanocomposites in this work have the lowest thermal conductivity reported for an inorganic nanostructure to date (0.16 $Wm^{-1}K^{-1}$).

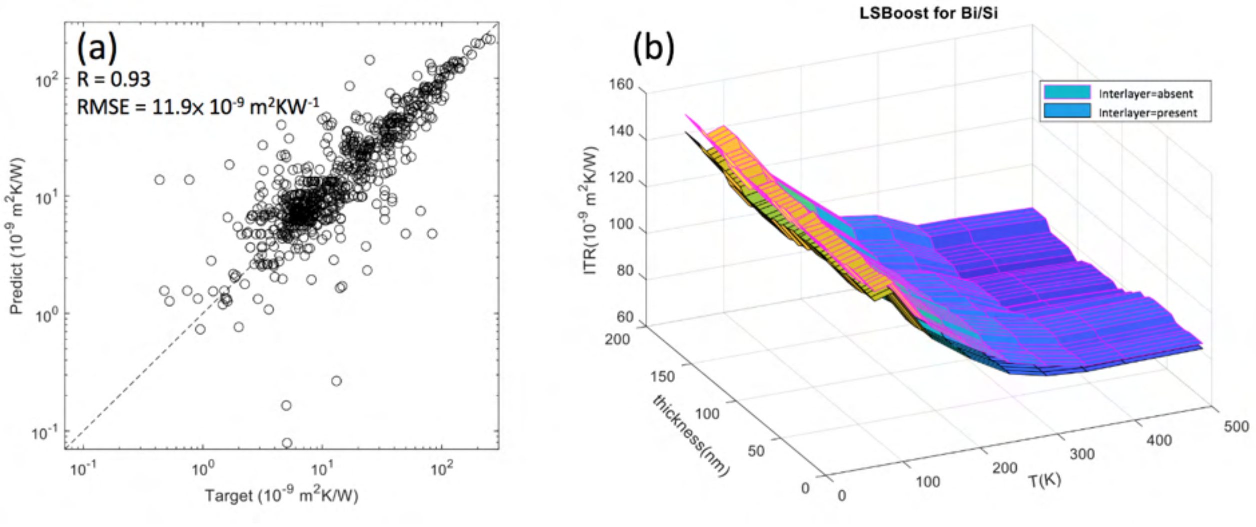
(a)
R = 0.93
RMSE = 11.9× 10-9 m2KW-1
Predict (10-9 m2K/W)
Target (10-9 m2K/W)
10-1
100
101
102
(b)
LSBoost for Bi/Si
Interlayer=absent
Interlayer=present
ITR(10-9 m2K/W)
160
140
120
100
80
60
thickness(nm)
200
150
100
50
0
T(K)
0
100
200
300
400
500

Figure 1

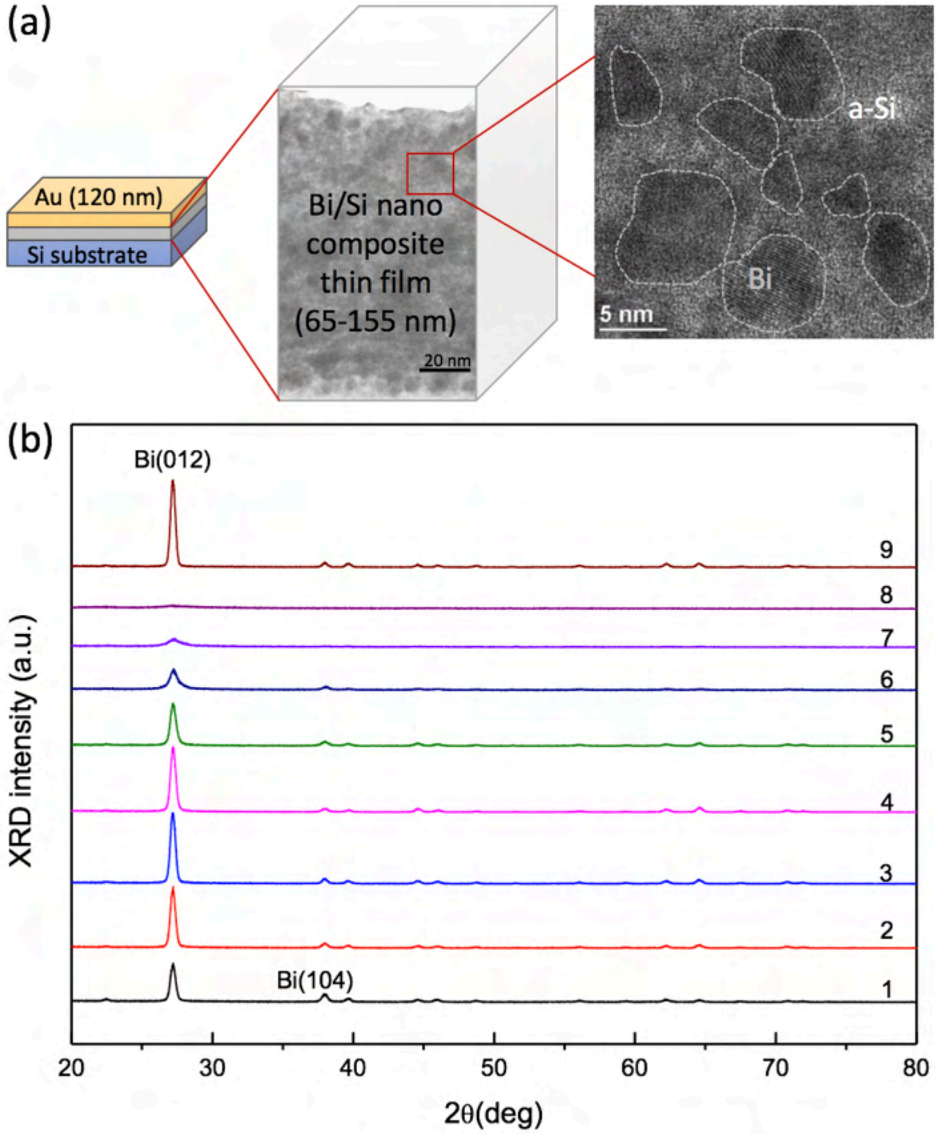
(a)
Au (120 nm)
Si substrate
Bi/Si nano composite thin film (65-155 nm)
20 nm
a-Si
Bi
5 nm
(b)
Bi(012)
Bi(104)
9
8
7
6
5
4
3
2
1
XRD intensity (a.u.)
20
30
40
50
60
70
80
2θ(deg)

Figure 2

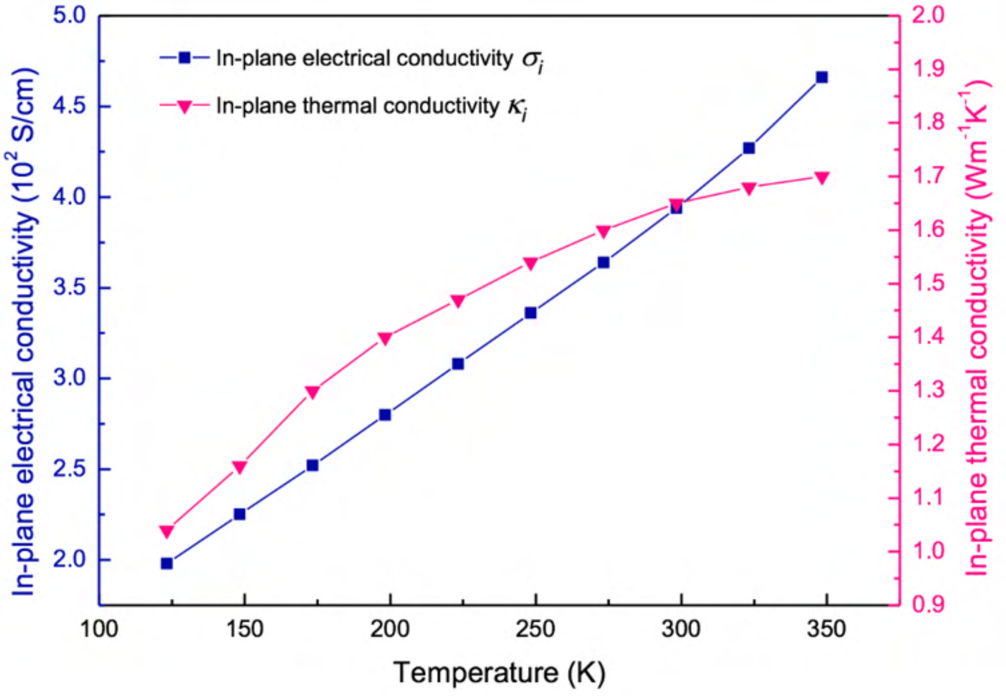
In-plane electrical conductivity σ_i
In-plane thermal conductivity κ_i
In-plane electrical conductivity (10^2 S/cm)
In-plane thermal conductivity ($Wm^{-1}K^{-1}$)
Temperature (K)
5.0
4.5
4.0
3.5
3.0
2.5
2.0
2.0
1.9
1.8
1.7
1.6
1.5
1.4
1.3
1.2
1.1
1.0
0.9
100
150
200
250
300
350

Figure 3

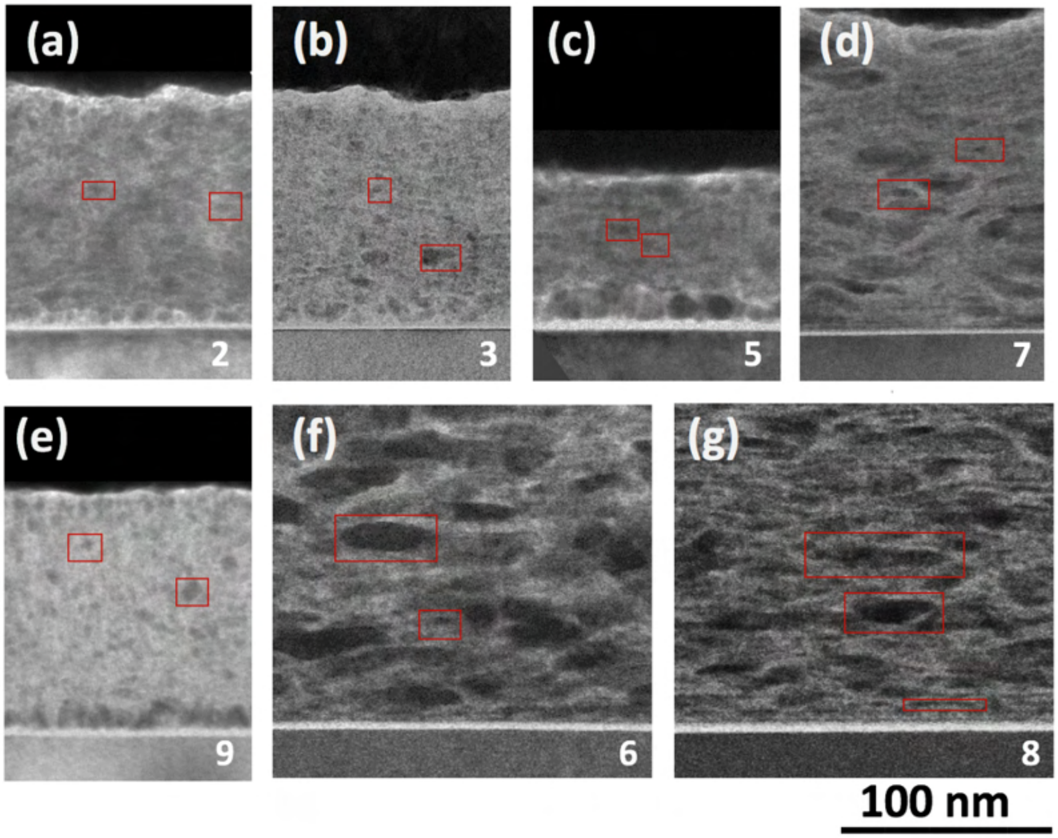

Figure 4

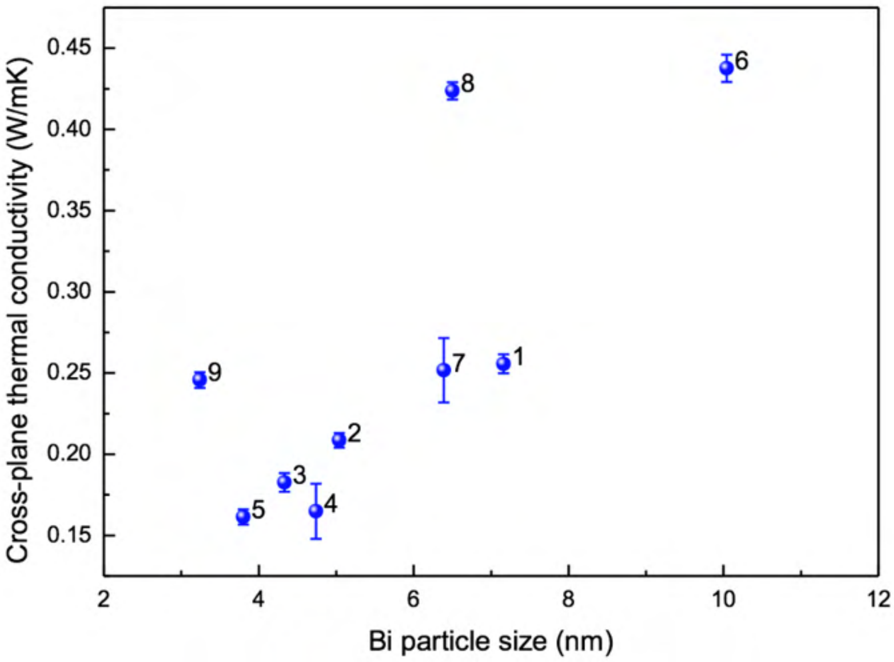

Figure 5

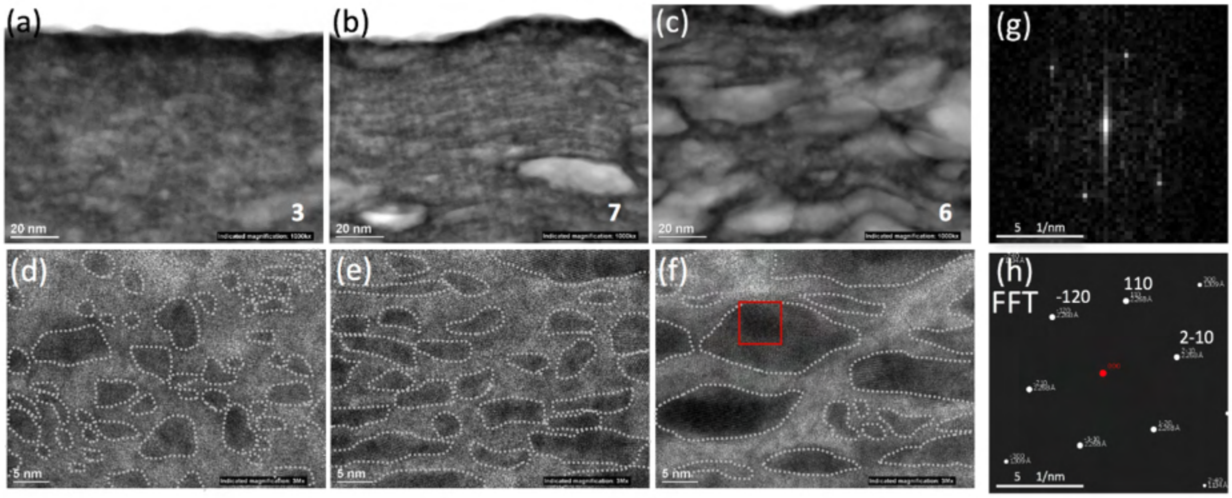

Figure 6

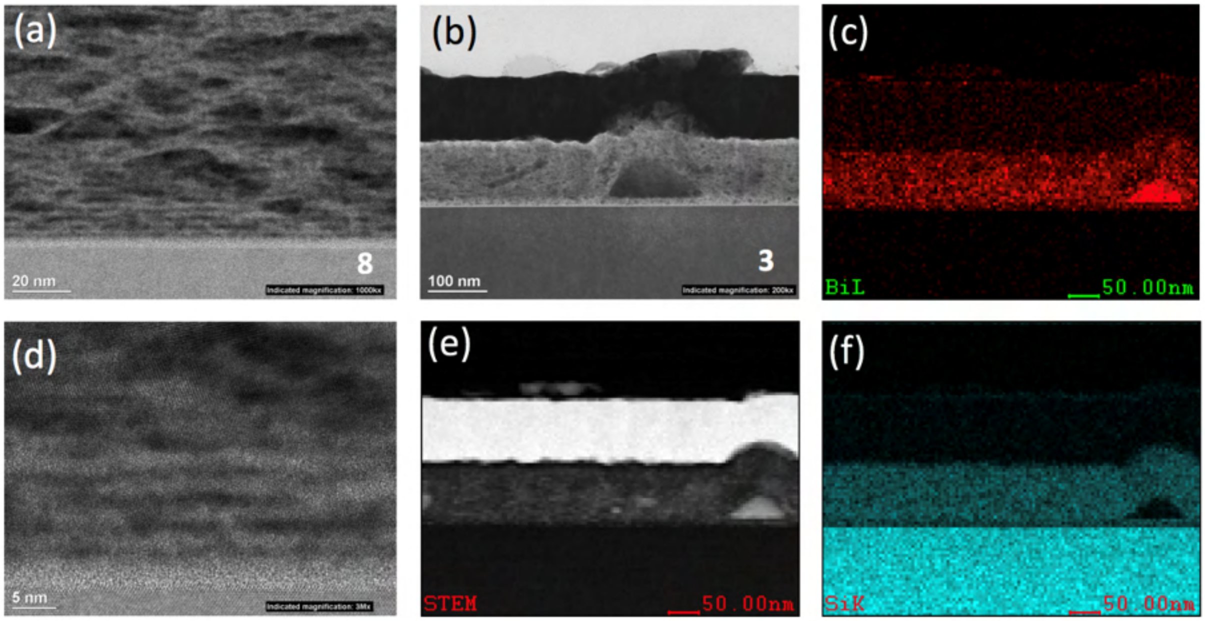

Figure 7

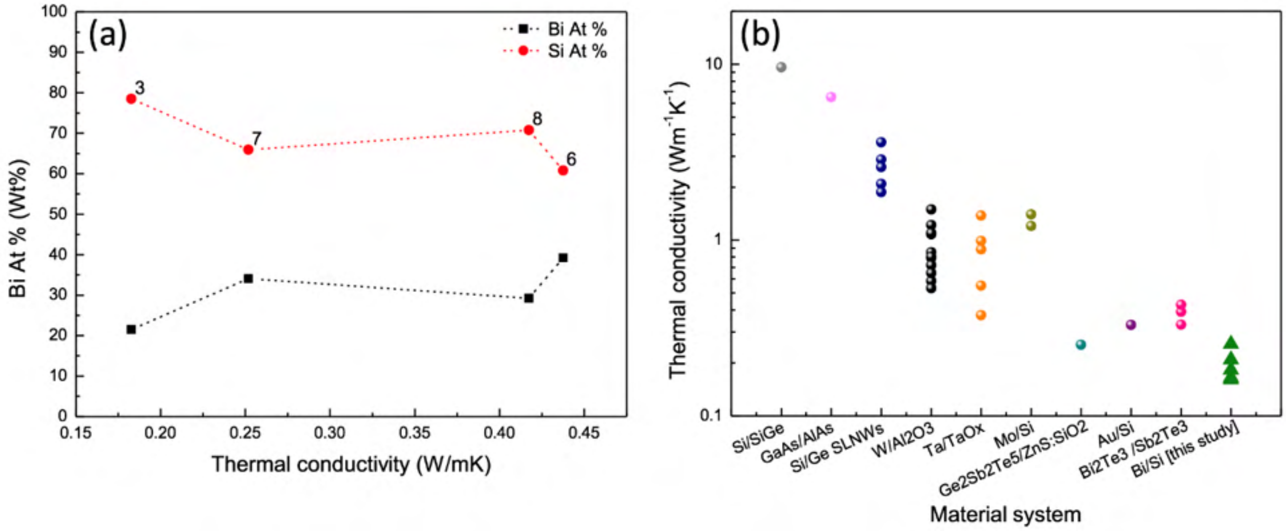

Figure 8

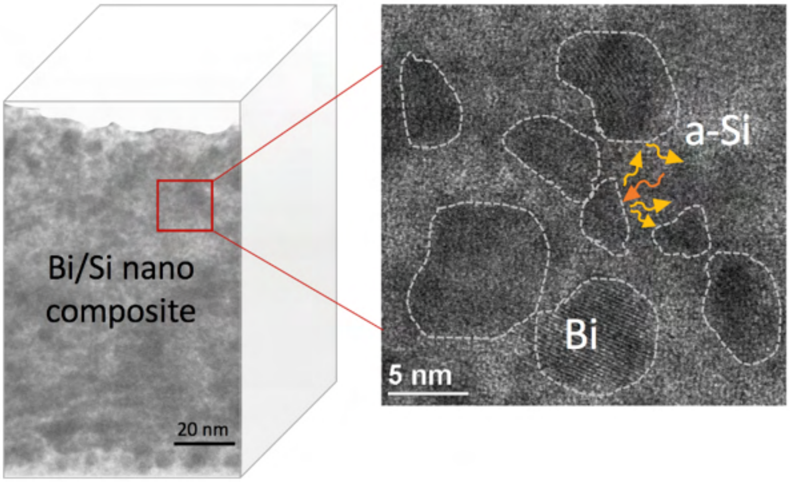

Graphic Abstract